Shadowgraphy investigations of high speed water jet atomization into still air

C. Stevenin, Séverine Tomas, A. Vallet, M. Amielh, Fabien Anselmet

Shadowgraphy investigations of high speed water jet atomization into still air

C. Stevenin*[1], S. Tomas[1], A. Vallet[2], M. Amielh[3] and F. Anselmet[3]
[1] LERMI, Irstea, 3275 route de Cézanne, 13182 Aix-en-Provence Cedex 5, France
[2] ITAP, Irstea, 361 rue J.F. Breton, 34196 Montpellier Cedex 5, France
[3] IRPHE, 49 rue F. Joliot Curie, B.P. 146, 13384 Marseille Cedex 13, France

Abstract

The present study aims at characterizing the atomization of a water jet which is injected at high velocity into still air thanks to an industrial nozzle particularly used in irrigation. The nozzle diameter is 4.36 mm and exit velocity is about 25 m/s. The droplet size and velocity are analyzed by a double-pulsed shadowgraph imaging technique using a Droplet Tracking Velocimetry (DTV) method and are compared with optical probe measurements. A particular attention is paid to the calibration of the imaging system to define the measurement volume associated with each droplet size and to improve the estimation of droplet diameters. The results of the calibration procedure are then used to estimate the size of non-spherical liquid fragments. Drop size distributions are obtained by image processing as a function of the turbulent scales of the upstream flow, as well as Reynolds and Weber numbers. Preliminary results show that log-normal distributions give the best fit to the experimentally observed drop size distributions. Moreover the ratio of the Mass Median Diameter (MMD) over the Sauter Mean Diameter (SMD) is found to be constant and equal to 1.2, which is in good agreement with previous studies, and yields to a relation between the mean and the standard deviation of lognormal distributions.

Introduction

Irrigation accounts for 70% of global water consumption. Among existing equipments, sprinkler irrigation is one of the most widely spread systems, particularly in Europe. It consists in discharging a high velocity water jet into still air, which disintegrates under the influence of its own turbulence and aerodynamic forces. The main drawback of this technique is that wind drift, evaporation or inadequate material design can result in a poor uniformity of the water application, which can lead to a decrease of farming productivity, water losses (pudding and streaming) and eventually negative impacts on farming parcel soil (erosion, soil leaching and compaction). To reduce irrigation water losses and improve water use efficiency, it is necessary to get a better knowledge of the mechanism involved in the water jet break-up, from the nozzle exit to the fully atomized spray.

At nozzle exit, ligaments are formed by the liquid turbulence. Aerodynamic effects are relatively small because of the high density ratio of the studied jet ([11],[14],[15]). Further, liquid colum is distorted by the turbulent large scales ([5],[10]). The influence of aerodynamic forces increases and eventually leads to the liquid column fragmentation, with secondary atomization mechanisms involved. A review of experimental results for large jet atomization, at high Reynolds and Weber number, can be found in [4]. The resulting spray is then constituted of relatively small droplets issued from bag break-up and shear break-up mechanisms, very large fragments coming from the liquid column fragmentation and intermediate size elements. The presence of non spherical elements and the large range of size of liquid elements in the spray are often a limit for experimental techniques. The main advantage of imaging, besides being a non-intrusive technique, is to overcome these difficulties. However the main drawbacks of imaging are the detection and the size estimation of unfocused droplets, as well as the determination of the volume in which droplets are detected. The present work aims at providing a robust calibration procedure to correct the apparent diameter of large droplets. The first part of this paper describes the experimental method, the calibration of the imaging system and eventually the main steps of the image processing for droplet detection and size estimation. Finally the method is applied on spray images and results are presented and compared with optical probe measurements.

Experimental method

A shadowgraph technique is carried out using a double pulse laser illumination (Litron Nd:YAG 132 mJ) and a 12-bit 2048×2048 pixel camera. The camera is equipped with a 105mm F2.8 DG macro lens (Sigma) and captures images with a field-of-view of $65 \times 65mm$. The time delay between two successive frames is $30\mu s$. The flash duration is around 4ns, what is sufficiently short to freeze water droplet motion. The distance between the camera and the focal plane is 500mm. Image resolution is about 30 pixels/mm. Data are collected at four axial positions (respectively at 550, 660, 780 and 890 nozzle diameters from the nozzle exit) and several radial positions

for covering the whole jet diameter. Each dataset is composed of 500 image couples. Test conditions are reported in Table 1. The field of view is large (65 mm wide) and some image areas are not sufficiently lighted. It has been necessary to apply a circular mask, which diameter D_{mask} is $55mm$, to only analyse the central and lighted zone. After masking, all background pixels have the maximum pixel value (FIG. 1). Droplet sizing and tracking are eventually performed using Matlab Image Processing Toolbox and Dantec DynamicStudio software.

Parameter	Range
Nozzle diameter (d_{nozzle})	4.36 mm
Exit velocity (u_0)	22-26 m/s
Density ratio (ρ_L/ρ_G)	840
Reynolds number $(Re_L = \rho_L u_0 d_{nozzle}/\mu_L)$	88,000 - 126,000
Weber number $(We_L = \rho_L u_0^2 d_{nozzle}/\sigma)$	27,000 - 46,000
Ohnesorge number $(Oh = \mu_L/(\rho_L \sigma d_{nozzle})^{1/2})$	0.0017 - 0.0019

Table 1. Test conditions

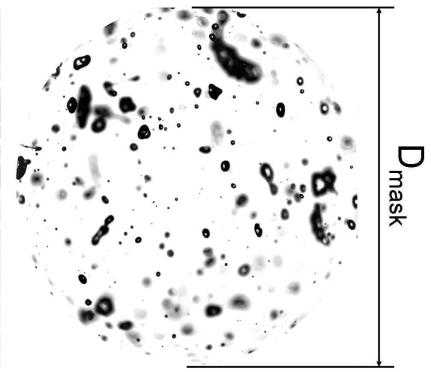

Figure 1. Exemple of spray image after masking

Calibration of the imaging system

Glass spheres were used for the calibration rather than water droplets to garantee a perfect reproductibility of the measurements. Glass spheres diameters d_0 ranged from 0.3mm to 10mm, with a precision of $+/-3\mu m$. During calibration experiments the camera and the light source were positioned vertically, whereas the glass spheres were placed on a glass slide on the optical axis. Images of the glass spheres were taken for different distances $|z|$ from the focal plane. A generic profile of pixel intensity values is presented (FIG. 2). Reference diameters D_l can be defined from a reference intensity i_{ref} corresponding to a relative level l on the profile:

$$i_{ref} = i_{min} + l * h \tag{1}$$

where h is the height of the profile $h = i_{max} - i_{min}$; i_{max} corresponds to image background (white) and i_{min} to the lower pixel value (dark).

Thereafter, $D_{l=25\%}$, $D_{l=50\%}$ and $D_{l=75\%}$ will respectively refer to diameters at 25%, 50% et 75% level on the intensity profile and we define the estimated diameter as the half-height diameter $D_{l=50\%}$. Large objects ($d_0 > 0.5mm$) on the focal plane are correctly sized (FIG. 3), with a sizing error less than 1%. However, a larger

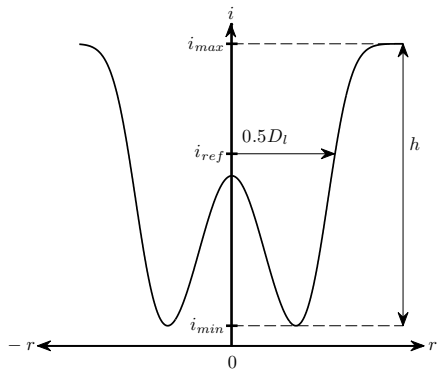

Figure 2. Generic profile observed for a transparent object

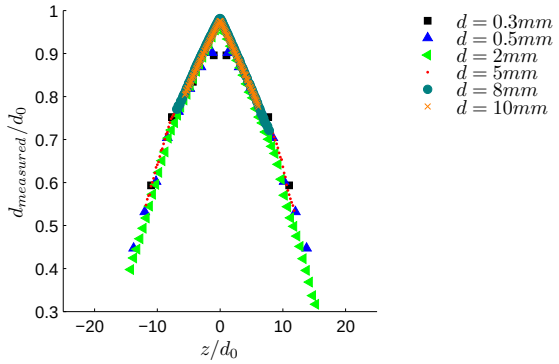

Figure 3. Ratio of the measured diameter $D_{l=50\%}$ to the real diameter d_0 at different defocus locations from the focal plane, without correction

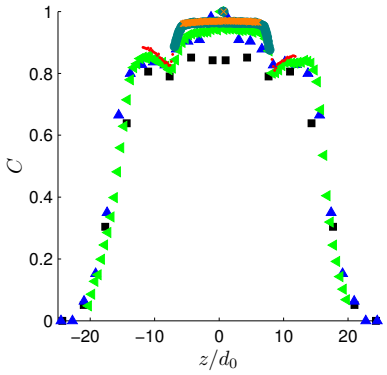

Figure 4. Variation of objects contrast with normalized distance from the focal plane

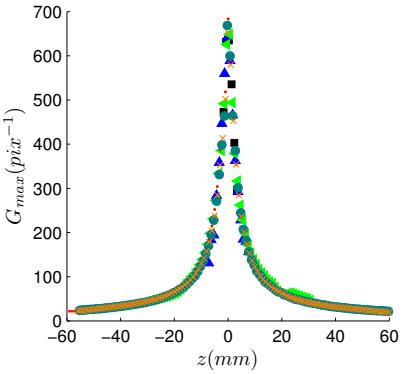

Figure 5. Maximum Intensity gradient on objects' border at different defocus locations from the focal plane

error is encountered for the smallest glass spheres ($d_0 \leq 0.5mm$), which is probably due to a lack of resolution in image discretization process. When defocusing, object diameters are more and more underestimated. The sizing error is an increasing function of $|z|/d_0$ and can reach up to 70%. This sizing error seems independent of the level l considered for the definition of the estimated diameter, what have been verified but is not reported here.

In order to limit sizing error, the classical method is to reject defocused objects. Most of previous works ([7],[8]) have proposed criteria based on gradient and contrast values to eliminate out-of-focus droplets. These methods lead to eliminate a number of droplets, especially the smallest ones, and reduce drastically the measurement volume since only objects very close to the focal plane are detected. Contrast, defined by Eq. (2), is a usual parameter to segregate the in-focus objects from out-of-focus ones [9] when these objects are small enough ($d_0 < 0.3mm$). However, in the case of large objects, the contrast remains at high values until a critical defocus distance at $|z|/d \approx 12$, which depends linearly on object diameter d_0, and drops abruptly further (FIG. 4).

$$C = \frac{i_{max} - i_{min}}{i_{max} + i_{min}} \tag{2}$$

Pixel gradient on object border (FIG. 5) is a better indicator of the defocusing distance for large objects [9]. A common way to compute the gradient of pixel values is to convolve images with a filter (Roberts, Sobel, Deriche operators, to name but a few). However, the result often depends on the filter characteristics. In our case, we only need the maximum of gradient values on the borders of each detected object, which can be robustly computed as:

$$G_{max} = \frac{h}{K\left(D_{l=75\%} - D_{l=25\%}\right)} \tag{3}$$

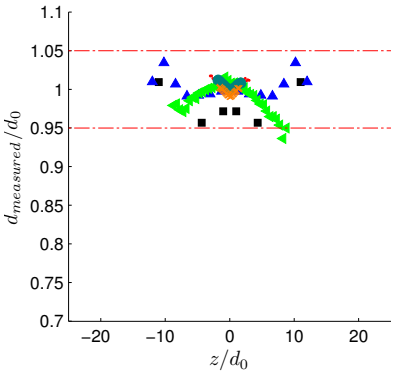

Figure 6. Ratio of the measured diameter $D_{l=50\%}$ to the real diameter d_0 at different defocus locations from the focal plane, after correction and segregation

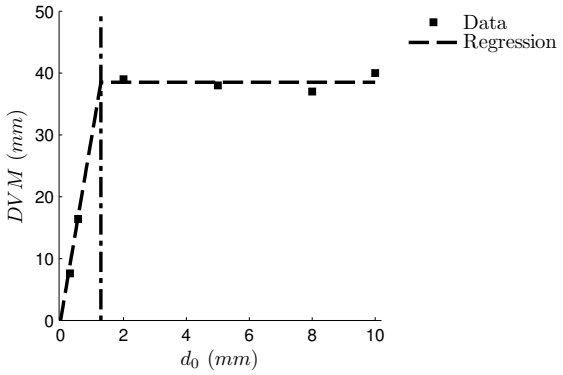

Figure 7. Depth of Volume Measurement DVM (mm) as a function of object diameter

where K is the number of pixels per unit length.

In this study, in order to keep a sufficient number of droplets, we propose to correct the estimated diameter thanks to our calibration dataset. The correction is based on experimental correlation between $D_{l=50\%}/d_0$ and gradient indicator parameter GI (Eq. (4)) which was proposed by Koh et al. [7] as an in-focus criterion for large objects ($d_0 > 0.3mm$):

$$GI = K\frac{D_{l=50\%} * G_{max}}{h} \tag{4}$$

where K is the number of pixels per unit length.

Two criteria are employed to reject very defocused droplets if their contrast or their GI value are respectively below a threshold contrast or lower than a predetermined limit value. Results of sizing after correction are represented in FIG. 6. For small droplets ($d_0 \leq 0.5mm$), it can be observed that the diameters are slightly overestimated. However the correction seems particularly robust since final sizing error never exceeds 5%.

Statistical corrections

In our algorithm, a droplet will be detected if its contrast and its GI parameter are respectively greater than fixed thresholds. These two limit values determine a measurement volume, which is found to vary linearly with droplet diameter for small droplets and to reach a constant value for the largest ones (FIG. 7). It can be linked with the fact that small droplet detection is controlled by the intensity threshold and large droplets detection by the GI parameter. Moreover, it is found that, if no criterion is applied for droplets discrimination, measurement volume is proportional to droplet diameter and detection is only limited by the contrast drop (FIG. 4). The dependance between measurement volumes and object sizes introduces a statistical bias and has to be taken into account in estimations of size distributions and droplet concentrations, which is done in our algorithm by dividing, in size histograms, each number of droplets N_i in size class i by the corresponding measurement volume.

Moreover, droplets across mask image border are rejected, which introduces also a bias since large droplets have statiscally more chance to touch mask border than small ones. To offset this effect, each size class i is weighted with a correction factor, calulated from the probability P for a droplet of diameter d_i to touch the border of a circular mask of diameter D_{mask}:

$$P = (D_{mask} - d_i)\, d_i / D_{mask}^2 \tag{5}$$

Droplet detection and sizing in spray images

Each droplet is firstly detected and then isolated from its surrounding by a mask. Most often this is done using a global threshold on intensity values. However this method leads to bad detections when droplets with different contrast values are overlapping or when droplets have several local minima in their intensity profile (large droplets). Moreover, if the threshold level is too high, a number of defocused droplets will not be detected. On the contrary if the threshold value is too low the background noise can lead to false positive events. To improve this

first detection step a technique based on wavelet transform has been employed ([1]). Once droplets are localized, a local analysis of intensity profiles is performed both to separate partially overlapping droplets and to determine droplet contrast, intensity gradient and contours. The droplet diameter D_A is usually calculated from the area A of the droplet shape as ([2]):

$$D_A = \sqrt{\frac{4A}{\pi}} \tag{6}$$

However this expression is not relevant in the case of non spherical droplets. Instead, the volume of a non spherical droplet is estimated using a method proposed by Daves et al. [3]. The droplet shape is divided into slices perpendicularly to its principal axis of inertia (FIG. 8). Each slice is supposed cylindrical and the droplet volume V is calculated as the sum of each slice volume. Finally the droplet diameter D_V is defined as:

$$D_V = \sqrt[3]{\frac{6V}{\pi}} \tag{7}$$

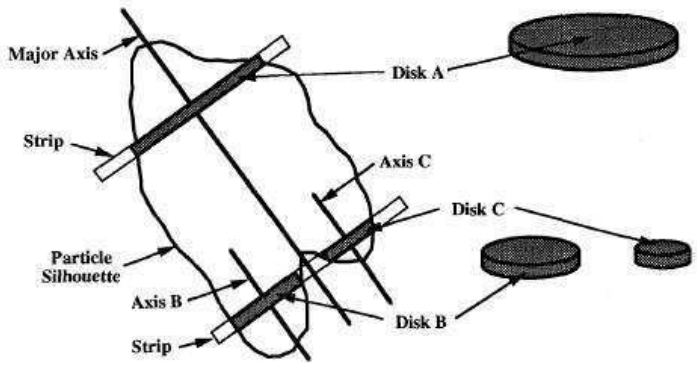

Figure 8. Volume reconstruction with cylindrical slices (Daves et al. [3])

Results

An optical probe is used for comparison with our imaging measurements. The probe tip is sensitive to the index of refraction and gives a different signal when it is surrounded by air or by water. The liquid volume fraction is determined from the proportion of time where the probe tip is in the water t_L over the total time $t_L + t_G$ (Eq. (8)). Moreover, droplets velocity can be measured from the rise time of the optical probe signal. Optical probes have already been used for experimental studies on irrigation water jets and have shown satisfactory results [6].

$$\tau = \frac{t_L}{t_G + t_L} \tag{8}$$

where t_G and t_L are respectively the time where the probe tip is in air and in water.

Void ratio

The liquid volume fraction is obtained from our image processing as :

$$\tau = \sum \frac{N_i \left(\frac{\pi D_{V,i}^3}{6}\right)}{\mathrm{VM}_i}, \tag{9}$$

where N_i is the number of droplets in the size class i, $D_{V,i}$ is the value at the center of the bin and VM_i is the corresponding measurement volume determined by calibration as $\mathrm{VM}_i = \mathrm{DVM}_i * (\pi D_{mask}^2/4)$. Results (FIG. 9 and FIG. 9) show a good agreement between the two measurement techniques for the two distances considered. The vertical and horizontal profiles obtained with the optical probe are quite identical, which suggests that the flow is more or less axisymmetrical. Experimentally more droplets are found below the jet axis than above it when gravity effects become playing a role. However in these zones, the spray is very dilute and these droplets do not seem to be very representative of the flow.

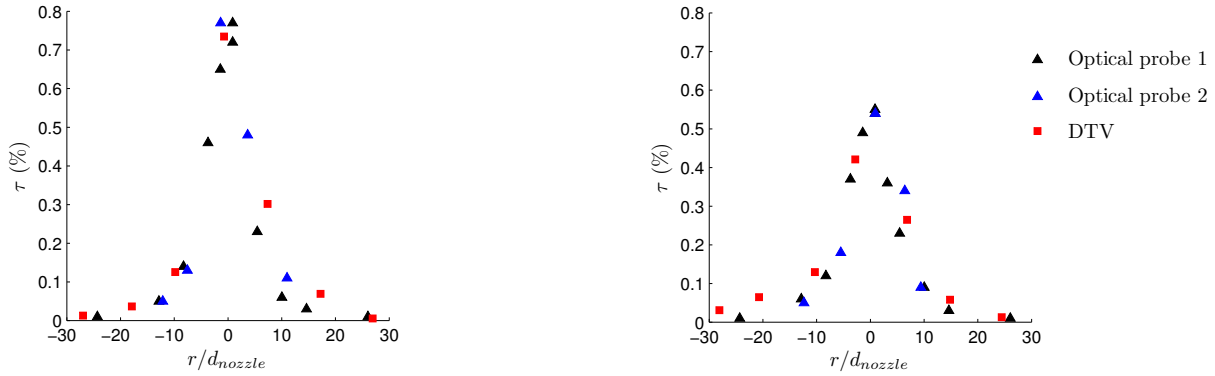

Figure 9. Comparaison of liquid volume fraction measurements at 780 (left) and at 890 (right) nozzle diameters from the nozzle exit; the first two datasets correspond to optical probe measurements (respectively on a horizontal then a vertical jet diameter), the last dataset is obtained by our imaging method

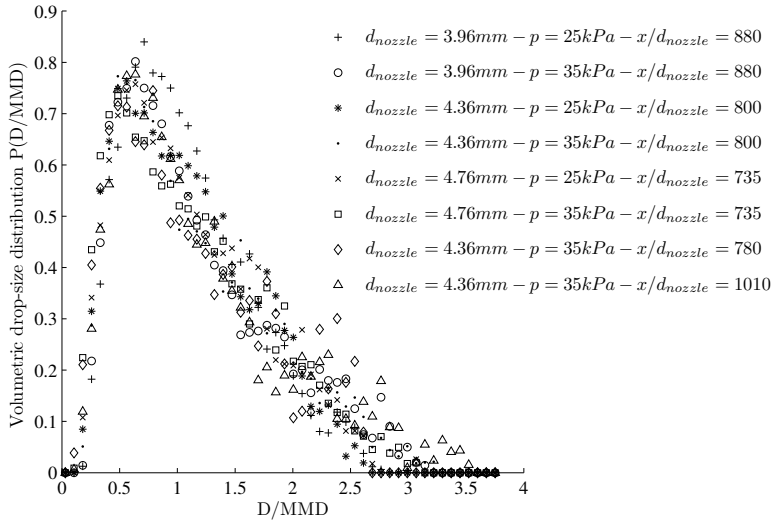

Figure 10. Experimental droplet size distributions obtained for different We_L and Re_L numbers and different distances from the nozzle

Droplet sizing

Volumetric drop size distributions for all test conditions are represented on FIG. 10 for distances from 735 to 1010 nozzle diameters from the nozzle. The same tendancy is observed for all the experimental conditions (FIG. 10). The lognormal law (Eq. (10)) is found to provide a very good fit to experimental distributions (FIG. 11), better than the root normal distribution proposed by [12]. Moreover, this lognormal law is only parametrized by the Mass Median Diameter since standard deviation of the distribution is related to the ratio of the Mass Median Diameter over the Sauter Mean Diameter (SMD) by Eq. (11). This ratio is found constant and equal to 1.2 (FIG. 12), which is in good agreement with previous studies ([12]).

$$P_V(D) = \frac{1}{\sqrt{2\pi}s_g D} exp\left(-\frac{[ln(D/\mathrm{MMD})]^2}{2s_g^2}\right) \tag{10}$$

$$s_g = 2ln\left(\frac{\mathrm{MMD}}{\mathrm{SMD}}\right) \tag{11}$$

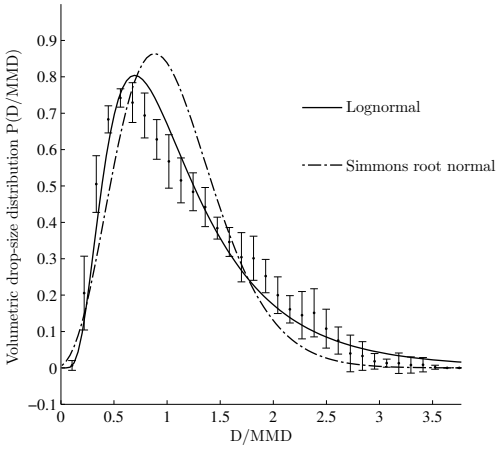

Figure 11. Experimental distributions - dots and errorbar represent respectively the mean and the standard deviation, per size class, of the experimental distributions reported in FIG. 10

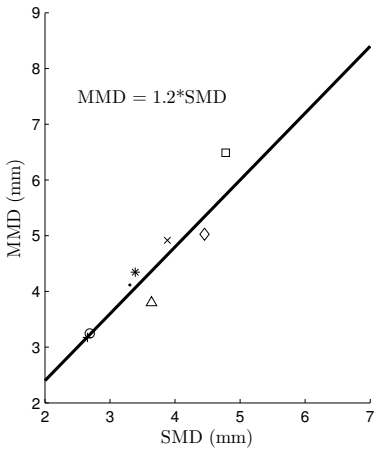

Figure 12. Median Mass Diameter (MMD) as a function of Sauter Mean Diameter (SMD), for the same experimental conditions as in FIG. 10

Velocities

Radial velocity profiles at 780 and 890 nozzle diameters from the nozzle are reported in FIG. 13 and in FIG. 13. Good agreement is found between the two methods and the same tendancies are observed. The maximum velocity is found on the jet axis and decreased radially (15m/s over 30 diameters) as the spray becomes more dilute. It can also be noticed that the boundary of the mixing layer is not reached and that more radial positions would be necessary to get a complete velocity profile.

Optical probe accuracy for velocity estimation is about 15% and is represented by errorbars on the plots. Moreover, optical probe measurements tend to overestimate large velocities, what could explain the differences observed near the jet axis in FIG. 13. The differences observed far from the spray axis are attributed to a lack of events in these dilute regions since experimental data for these radial positions are not always well converged.

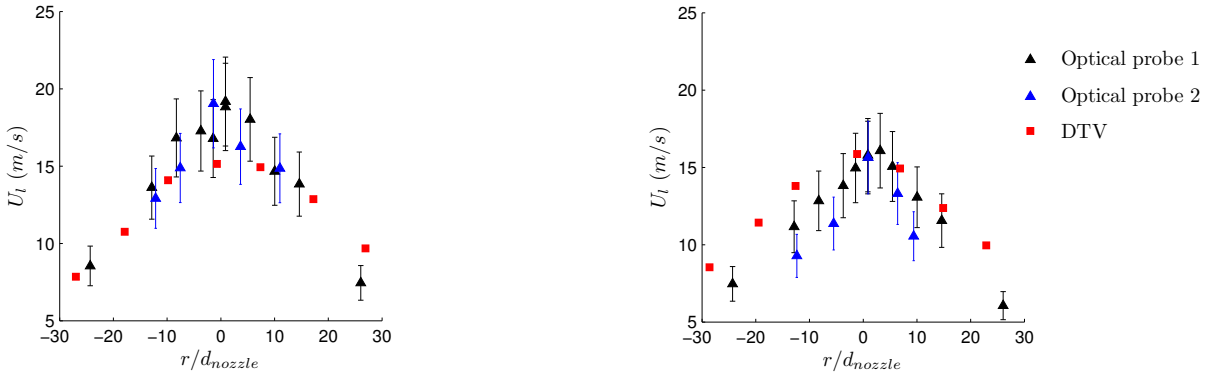

Figure 13. Comparaison of liquid velocity (magnitude) at 780 (left) and at 890 (right) nozzle diameters from the nozzle exit; the first two datasets corresponds to optical probe measurements (respectively on a horizontal then a vertical jet diameter), the last dataset is obtained by our imaging method

Summary and Conclusions

An image processing technique has been developed to take into account the dependance of the measurement volumes on droplets diameter as well as corrections of the apparent diameter of unfocused droplets. The technique has then been applied on an irrigation water jet and has been successfully compared with optical probe measurements for liquid volume fraction and droplets velocity profiles at two distances from the nozzle. Results show that volumetric drop size distributions have the same shape and can be correctly represented by a lognormal distribution. Moreover the ratio of the Sauter diameter (SMD) over the Mass Median Diameter (MMD) is found to be

constant and equal to 1.2, which is in good agreement with previous studies, and yields to a relation between the mean and the standard deviation of the lognormal distributions.

The validation of the axisymmetric assumption is in progress by getting volume flux distribution using a mechanical patternation technique.

Acknowledgements

This study is partly supported by the Région Provence-Alpes-Cotes d'Azur and the European Union (ERDF).

References

[1] Blaisot, J. B., Yon J., *Experiments in Fluids* 39(6):977-994 (2005)
[2] Chigier, N., *Progress in Energy and Combustion Science*, 17:211-262 (1991)
[3] Daves, G. G, Buckius, R. O., Peters, J. E, and Schroeder A. R., *Aerosol Science and Technology*, 19(2):199-212 (1993)
[4] Dumouchel, C., *Experiments in Fluids*, 45(3):371-422 (2008)
[5] Hoyt, J.W, Taylor, J.J, *Journal of Fluid Mechanisms*, 83(1):119-127 (1977)
[6] Kadem, N., Tchiftchibachian, A., and Borghi, R., *Atomization and Sprays*,18(4):315-341 (2008)
[7] Koh, K. U., Kim, J. Y., Lee,S. Y., *Atomization & Sprays* 11(4):317-333 (2001)
[8] Lecunoa, A., Rodriguez P. A, Sosa, P. A, and Zequeira, R. I, *Measurement Science and Technology* 11(8):1152-1161 (2000)
[9] Lee, S. Y, Kim, Y. D, 9^{e} *ICLASS Proceeding* (2003)
[10] Sallam, K. A, Dai, Z., and Faeth, G. M, *International Journal of Multiphase Flow*,28(3):427-449 (2002)
[11] Sallam, K. A, Faeth G. M, *AIAA journal*,41(8) (2003)
[12] Simmons H. C, *ASME Journal of Engineering for Power*, 99:309-319 (1977)
[13] Vallet, A., Burluka, A., and Borghi, R., *Atomization and Sprays*, 11(6):619-642 (2001)
[14] Wu, P. K., Tseng, L. K. and Farth G. M., *AIAA, Aerospace Sciences Meeting and Exhibit, 30th, Reno, NV* (1992)
[15] Wu, P. K., Faeth, G. M., *AIAA, Aerospace Sciences Meeting and Exhibit, 31st, Reno, NV* (1993)